Modelling and Simulation in Materials Science and Engineering

PAPER • **OPEN ACCESS**

Efficient determination and evaluation of steady-state thermal–mechanical variables generated by wire arc additive manufacturing and high pressure rolling

To cite this article: Valeriy Gornyakov *et al* 2022 *Modelling Simul. Mater. Sci. Eng.* **30** 014001

View the article online for updates and enhancements.

You may also like

- Wire Arc Additive Manufacturing Perspectives and Recent Developments
V Dhinakaran, B Stalin, M Ravichandran et al.
- 316L WAAM and pressure machining influence
Xinfeng Kan, Dengcui Yang, Zhengzhi Zhao et al.
- Challenges associated with the wire arc additive manufacturing (WAAM) of aluminum alloys
Shivraman Thapliyal



IOP ebooks™

Bringing together innovative digital publishing with leading authors from the global scientific community.

Start exploring the collection–download the first chapter of every title for free.

This content was downloaded from IP address 86.180.108.80 on 11/01/2022 at 14:25

OPEN ACCESS
IOP Publishing
Modelling and Simulation in Materials Science and Engineering
Modelling Simul. Mater. Sci. Eng. **30** (2022) 014001 (27pp) https://doi.org/10.1088/1361-651X/ac35b8

Efficient determination and evaluation of steady-state thermal–mechanical variables generated by wire arc additive manufacturing and high pressure rolling

Valeriy Gornyakov, Yongle Sun*, Jialuo Ding and Stewart Williams

Welding Engineering and Laser Processing Centre, School of Aerospace, Transport and Manufacturing, Cranfield University, Cranfield, MK43 0AL, United Kingdom

E-mail: yongle.sun@cranfield.ac.uk

Received 23 June 2021, revised 1 October 2021
Accepted for publication 2 November 2021
Published 20 December 2021



Abstract

Wire arc additive manufacturing (WAAM) of large component is susceptible to residual stress (RS) and distortion, which are detrimental and need to be mitigated through high pressure rolling or other methods. In this study, an efficient modelling approach is developed to simulate both WAAM and rolling, and this approach can also be applied to other manufacturing processes to determine steady-state variables. For a clamped wall component, the computationally efficient reduced-size WAAM and rolling models (i.e. short models) can obtain steady-state solutions equivalent to those obtained by conventional full-size models. In the short models, the undesirable effect of reducing the length of the modelled component is counteracted by imposing additional longitudinal constraint as proper to specific processes. The steady-state solution obtained by the short model in clamped condition is then mapped to a long model for analysis of RS and distortion after removal of clamps. The WAAM model predictions of temperature, RS and distortion are in good agreement with experimental measurements. For the steady-state region in the WAAM deposited wall, compressive longitudinal plastic strain (PS) is approximately uniformly formed, and the influential factors and implications of the PS are analysed. The high pressure rolling on the wall after WAAM deposition introduces tensile PS that compensates for the compressive PS induced by the WAAM deposition,

*Author to whom any correspondence should be addressed.



Original content from this work may be used under the terms of the Creative Commons Attribution 4.0 licence. Any further distribution of this work must maintain attribution to the author(s) and the title of the work, journal citation and DOI.

thereby mitigating the tensile RS in the clamped wall and alleviating the bending distortion after the removal of clamps. This study demonstrates an efficient approach for modelling large-scale manufacturing and provides insights into the steady-state strains and stresses generated by WAAM and rolling.

Keywords: large-scale additive manufacturing, rolling, residual stress, distortion, plastic strain, simulation

(Some figures may appear in colour only in the online journal)

1. Introduction

Wire arc additive manufacturing (WAAM) is an emerging variant of additive manufacturing (AM) technology, which can build medium- to large-scale fully-dense complex components with functional structural integrity [1–3]. WAAM with high deposition rate, which can be 9.5 kg h^{-1} for martensitic stainless steel [4] and most practically, 1–4 kg h^{-1} for aluminium and steel [1], provides rapid and economical route to large-scale AM. Using WAAM processes, large components were built from steel [5], titanium alloy [6], nickel superalloy [7], aluminium alloy [8], tantalum [9], tungsten [10], etc, and functionally graded structures were also printed using refractory metals [11]. The modular design of WAAM process utilises standard welding equipment and wire consumables, and hence allows low build-up and operational cost [1, 3, 12]. Moreover, a range of cold working can be integrated in WAAM systems. For instance, high pressure rolling was recently combined with WAAM to introduce some beneficial effects, such as mitigation of residual stress (RS) and distortion [5], microstructural refinement or modification [5, 13], elimination of porosity [8], and improvement of mechanical properties [14, 15]. Despite the experimental evidences of the benefits brought by rolling, the underlying mechanisms responsible for such benefits are complex and need to be understood. Unfortunately, experimental measurements are limited and difficult to provide adequate information for establishing the understanding. Therefore, modelling is crucial for gaining better insights.

WAAM-built components are susceptible to RS and distortion [5, 6], which are major challenges that hinder the wider applications of WAAM in industry. RS arises from the process-induced plastic strain (PS), among other incompatible deformation, as generated during the thermal cycles caused by WAAM deposition. Distortion usually occurs when the RS is partially released after the removal of clamps on the WAAM-built component, while it can also occur during the WAAM process due to the deformation induced by the temperature changes. RS is usually detrimental and can lead to early fatigue failure, stress corrosion cracking and brittle fracture [16–19], while excessive distortion reduces process stability and geometrical precision. Therefore, determination and mitigation of RS and distortion is one of the main aims in WAAM research.

Thermal–mechanical finite element analysis (FEA) models prove a robust numerical tool to determine temperature, RS and distortion in WAAM [20–27]. However, the thermal–mechanical models are strongly nonlinear, and require fine meshes and small time increments to obtain accurate solution, meaning that the computational time can be too long to be practical for analysis of large WAAM-built components. As reported by Ding *et al* [20], a 3D transient thermal–mechanical model for a 20-layer 500 mm long WAAM-deposited wall took 75 h to obtain a solution using high-performance computing (HPC) facility. Such long computational time of conventional FEA model may not be acceptable for industrial WAAM components which can be several metres long. Thus an efficient modelling approach is needed.

Several efficient FEA modelling techniques have been developed in the allied fields of welding, powder-based AM and WAAM. A straightforward approach to reduce computational time is the use of graded mesh or adaptive meshing to reduce the number of the elements (and hence the degrees of freedom) in the thermal–mechanical model [20, 25]. The efficiency gained through this approach is compromised by the effort/time spent in meshing and the spatial resolution required for the analysis. Another approach is the simplification of 3D problems into 2D problems. Camilleri *et al* [28] used a 2D transient thermal model to predict the temperature distribution in a section transverse to the welding direction. However, a 2D thermal model does not consider longitudinal heat flow, which is usually significant during WAAM deposition. An Eulerian model is efficient to obtain steady-state temperature field. Zhang and Michaleris [29] and Ding *et al* [20] created Eulerian steady-state thermal models in which the heat source remained stationary and was attached to the Eulerian reference frame, while material flowed through the finite element mesh. The Eulerian model can be two-order faster than the conventional Lagrangian model, but its implementation for mechanical analysis is often sophisticated due to complicated mathematical formulation required [29, 30]. For efficient mechanical analysis, Michaleris and DeBicarry [31, 32] developed a PS-based method to predict distortion in large-scale welded thin-walled structures. The method is a variant of inherent strain method, which is based on elastic analysis using the sum of nonelastic strains as inherent strain, as originally proposed by Ueda *et al* [33, 34] for welding analysis. Recently, Chen *et al* [35] implemented inherent strain method for multilayer deposition by direct metal laser sintering AM. However, some limitations of the inherent strain method have been identified for powder-based AM processes when small-scale thermal–elastic–plastic model is used to determine the inherent strain [36, 37].

The FEA-based determination and evaluation of RS and distortion becomes more challenging when WAAM is combined with rolling. The rolling simulation for large components is also computationally demanding. It was shown that conventional FEA simulation of single-pass rolling on a 456 mm long weld took 95.3 h using HPC facility [38]. For efficient modelling of high pressure rolling, Gornyakov *et al* [39] demonstrated that a 3D implicit analysis model with reduced component length predicted steady-state RS and PS equivalent to the solution of a conventional full-size model, but the computational time was significantly reduced. Gornyakov *et al* [39] also examined a number of other efficient modelling techniques for rolling, including explicit analysis, Eulerian steady-state model and 2D simulation, and they found that the short model using implicit solution algorithm is the best option for rolling simulation when both efficiency and accuracy are required. However, Gornyakov *et al* [39] did not investigate the effects of longitudinal constraint on the predictions by the short model, nor the transfer of short model solution to the full-size component for further analysis of material response to clamps removal. Simulations of rolling for clamped WAAM components have been also attempted by Abbaszadeh *et al* [40] and Tangestani *et al* [41].

Most of previous research focussed on the development of efficient modelling methods and analyses for individual manufacturing processes, such as WAAM [20, 21] and rolling [39]. It still needs a general approach to enable efficient modelling and evaluation of the combined process of WAAM and rolling. Previous studies have shown that steady state exists for many manufacturing processes. For instance, steady-state temperature fields were experimentally and numerically observed during blown-powder laser AM [42], steady-state thermal–mechanical response to WAAM deposition was confirmed by transient WAAM models [20, 21], steady-state plastic flow was predicted by deep cold rolling model [43], and rolling on WAAM parts reached steady state within short distance to the start boundary [39, 40]. Therefore, it is hypothesised that steady-state variables such as temperature, strains and stresses,

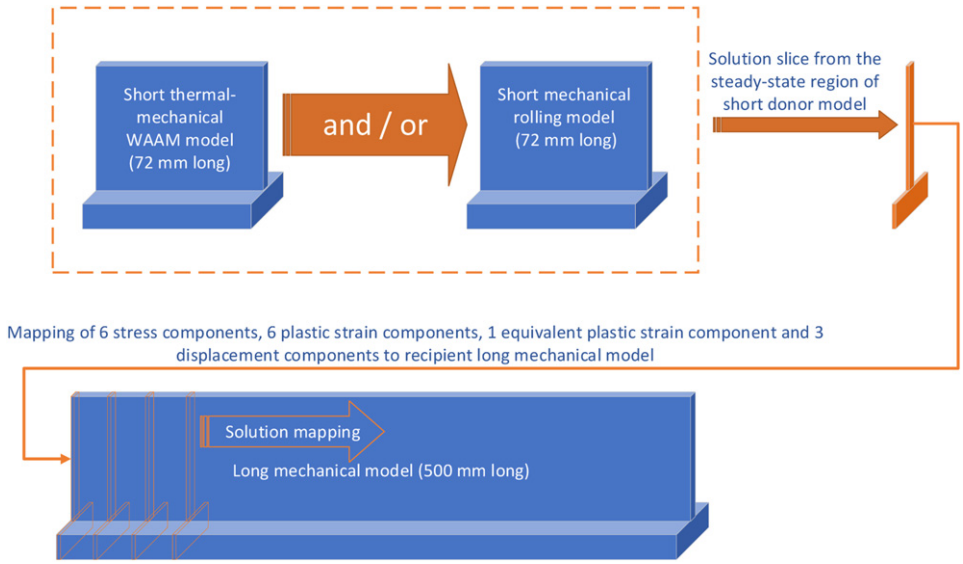


Figure 1. Schematic diagram of the proposed efficient modelling approach for determining steady-state thermal–mechanical variables using short models of WAAM and rolling, followed by mapping solution to long model for further analysis.

which are of major interest for process analysis, can be obtained using a technique in the same modelling framework.

This study is aimed to develop an efficient modelling approach applicable to both WAAM and rolling, thereby gaining insights into the mechanism of rolling-enabled mitigation of WAAM-induced RS and distortion. The computational efficiency is enhanced through reducing component length in the model. To compensate for the length reduction, proper longitudinal constraint is imposed in the short model to obtain the steady-state strains and stresses. Then the steady-state solution is mapped into a full-size long model to carry out mechanical analysis for the whole component after removal of clamps. In particular, the process-induced PS distribution is investigated, which is the main cause of RS and affects the distortion.

2. Modelling and verification/validation methods

2.1. Efficient method to simulate steady state of WAAM and rolling

Previous research showed that the WAAM [20, 21] and rolling [39] processes operating on clamped walls can attain a steady state within a certain distance along the travelling direction of the arc and roller (i.e. longitudinal direction), within which the PS and RS distributions are independent of longitudinal position. This means that a short transient model with reduced component length could be used to obtain the steady-state variables and save computational time. However, the steady-state solution obtained by the short model cannot be used for analysis of the effects of clamps removal on final RS and distortion, for which a full-size long model is still needed, since the self-constraint associated with the final state is dependent on the actual length of the component after the removal of clamps.

Figure 1 shows the efficient modelling approach proposed here to determine the steady-state physical variables generated by WAAM and rolling, as well as the final RS field and distortion

in the component. Firstly, a short model is created to determine the steady-state solution. For the WAAM and rolling processes considered in this study, a component length of 72 mm was found to be sufficient to attain the steady state. Secondly, the steady-state solution of the short model is mapped to a long mechanical model (the full length of the component is 500 mm for the WAAM and rolling studied here). The solution slice obtained from the steady-state region in the short model is repeatedly in space mapped to the long mechanical model using a solution mapping technique (section 2.2). The initial shape of the component in the mapped long model depends on the displacement solution of the short model. Thirdly, the final RS and distortion after removal of clamps are obtained using the long mechanical model.

The mapping of the steady-state solution from the short model to the long model is feasible thanks to the following two facts. First, the short model with proper boundary condition can reproduce the physical variables in the steady-state region of the original component (evidence will be presented in the results section). Second, after steady-state solution mapping, new stress equilibrium will be established in the long model due to the differences in the component length and boundary condition between the short model and the long model; nevertheless, this new equilibrium hardly affects the physical variables in the steady-state region, and the confirmation of this will be presented in the results section.

2.2. Solution mapping technique

Abaqus FEA software [44] was used for the WAAM and rolling simulations. A solution mapping technique was developed to transfer the solution from the short mechanical model to the long mechanical model, while the standard functions of Abaqus software do not support the transfer of equivalent solution between models with different lengths.

The Abaqus keyword of *INITIAL CONDITIONS was used to define the initial state of the long mechanical model using external text files, which contain a list of elements with predefined initial parameters. Element numbers were assigned in a controlled manner during meshing, except in the substrate where the transition from fine mesh to coarse mesh is complicated and the mesh topology may not be identical in the longitudinal direction. The six components of stress tensor, six components of PS tensor and the equivalent PS were extracted from the solution slice perpendicular to the longitudinal direction in the steady-state region of the short mechanical model (donor). A Python script was developed to generate the initial conditions, in which the extracted solution slice was assigned sequentially in space to the corresponding elements of each transverse section of the long mechanical model (recipient). For the substrate with complicated mesh topology, average values of stress and PS were obtained from the short model and predefined to the long model. This simplification was necessary for the substrate since the controlled node numbering was not conducted in this region, and thus the distribution of mapped variables is assumed to be uniform in this region of the recipient model. The Abaqus Keywords of ∗INITIAL CONDITIONS STRESS, PS and HARDENING were added to the recipient model. As isotropic hardening was adopted in the plasticity model for this study, only equivalent PS was transferred, while back stress could be also mapped when kinematic hardening model is used. A calculation of stress rebalancing was carried out in the recipient model with the predefined initial conditions and clamps, followed by the prediction of mechanical response to the removal of the clamps. It should be mentioned that elastic strain solution does not need mapping since the stress and elastic strain are conjugated.

For the long WAAM mechanical model, the displacement solution was not mapped because negligible distortion was predicted by the short WAAM mechanical model under clamped

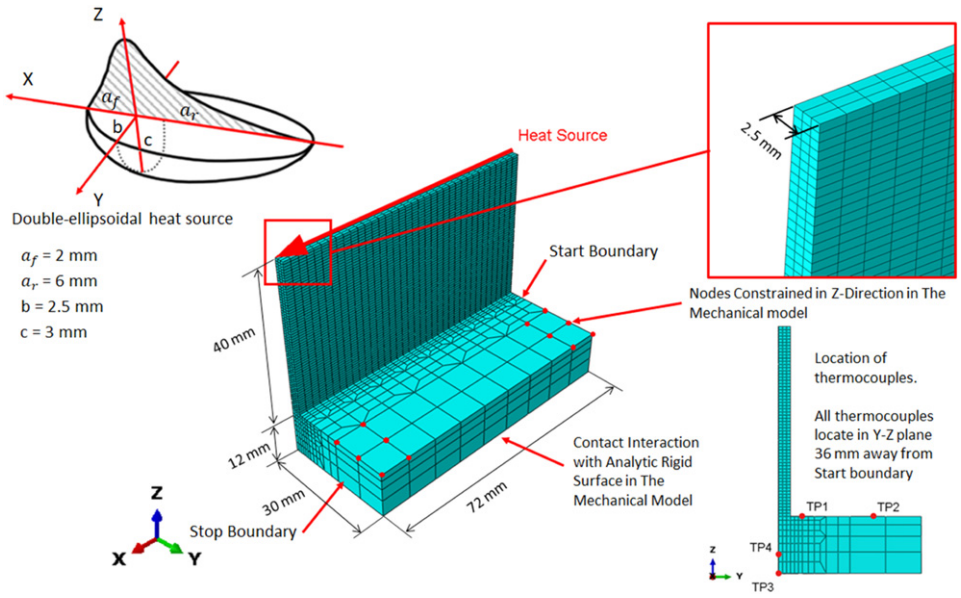


Figure 2. Short transient thermal–mechanical model of 20-layer WAAM-deposited wall with reduced length compared to the samples in previous experiments [20, 23]. The schematic of double-ellipsoidal heat source is also shown. The coordinates (in mm) of the thermocouples are TP1 (36, 5, 12), TP2 (36, 20, 12), TP3 (36, 0, 0) and TP4 (36, 0, 4). The *Y* coordinate of the symmetry plane and the *Z* coordinate of the substrate bottom are both zero.

condition, while for the long rolling model the displacement mapping was performed because considerable deformation occurred in the simulation using the short rolling model.

2.3. WAAM model and validation method

The proposed efficient modelling approach was applied to WAAM deposition of a mild steel (S355) wall (figure 2). The validation of the WAAM model was based on previous experiments by Ding *et al* [20, 23] and Colegrove *et al* [5], and the details of the experiments can be found in the references. A short multilayer model was used for thermal–mechanical analysis of WAAM deposition. The transient temperature field was predicted by a short thermal model and then the thermal solution was transferred to a short mechanical model. Only half of the wall and substrate was considered in the model due to symmetry.

The double-ellipsoidal moving heat source model [45] was employed in the thermal analysis, which was implemented using Abaqus user defined subroutine DFLUX. The power density in the front region of the heat source is expressed as

$$q_{\mathrm{f}} = \frac{6\sqrt{3}f_{\mathrm{f}}Q}{\pi\sqrt{\pi}a_{\mathrm{f}}bc}e^{\left[-3\left(\frac{(x-vt)^2}{a_{\mathrm{f}}^2}+\frac{y^2}{b^2}+\frac{z^2}{c^2}\right)\right]}. \tag{1}$$

And in the rear region, we have

$$q_{\mathrm{r}} = \frac{6\sqrt{3}f_{\mathrm{r}}Q}{\pi\sqrt{\pi}a_{\mathrm{r}}bc}e^{\left[-3\left(\frac{(x-vt)^2}{a_{\mathrm{r}}^2}+\frac{y^2}{b^2}+\frac{z^2}{c^2}\right)\right]}. \tag{2}$$

Where f_f and f_r are the heat distributing factors for the front and rear regions, respectively, which satisfy the condition that $f_f + f_r = 2$; Q is the power input (absorption efficiency is considered); v is the travel speed of the heat source and t is travel time; a_f and a_r represent the lengths of the front and rear regions, respectively; and b and c are the lateral and vertical radii of the heat source, respectively. The heat source parameters were adopted from references [20, 23] and are also shown in figure 2.

Simplified element 'birth' technique was used to simulate the deposition of a whole layer each time. Ding *et al* [21] found that the activation of the whole layer each time, instead of only activating the elements within the heat source radii, barely affects the solution accuracy.

Temperature-dependent material properties reported in reference [31] were used in the thermal model. The thermal conductivity at temperatures higher than the melting point (1500 °C) was artificially increased to reflect the convective heat transfer in the molten pool. Eight-node linear heat transfer brick elements (Abaqus designation DC3D8) were used in the thermal model. The mesh density gradually changed from being fine in the deposited wall (element size was 2 mm × 0.833 mm × 0.667 mm) to being coarse in the substrate (element size was 8 mm × 7.5 mm × 1.765 mm). The coefficient of convection and the emissivity of radiation for all free surfaces were 5.7 W m^{-2} K^{-1} and 0.2, respectively, while the heat loss due to the water-cooled backing plate was simulated by imposing convection with a coefficient of 300 W m^{-2} K^{-1} on the bottom of the substrate. To minimise the component end effect within short distance and focus on the steady-state region, the heat transfer on the start and stop boundaries was neglected in the short thermal model.

The mechanical model has the same dimensions and mesh topology as the thermal model. The element type was 3D stress eight-node linear brick with reduced integration (Abaqus designation C3D8R). Temperature-dependent elasto-plastic properties were adopted from reference [31], while solid state phase transformation was not taken into account, because for mild steel it does not play a significant role in RS [46]. Two sets of material properties were used for the substrate and deposited wall, respectively [31]. It should be mentioned that Colegrove *et al* [5] found that the peak longitudinal RS near the interface between the substrate and deposit reached 600 MPa. This finding suggests that the actual value of yield strength of WAAM deposited wall could be larger than the 450 MPa for mild steel at 20 °C reported in reference [31]. In the present model, the values of mild-steel yield strength as suggested by reference [31] were increased by 50 MPa for the wall deposit at the temperature range of 20 °C–500 °C to reflect the actual yield strength inferred from the experiments for the WAAM-built component.

A surface-to-surface contact interaction was specified between the bottom of the substrate and an analytic rigid shell simulating the backing plate. Six nodes in each corner of the top surface of the substrate were constrained in the vertical direction in order to simulate the clamps (figure 2).

The short model with reduced component length has lower resistance to longitudinal deformation compared to the actual deposited wall. For this reason, additional longitudinal constraint was applied to the short model and the influences of different constraint conditions on predicted PS and RS were investigated. Three types of longitudinal constraint were considered in the short model, i.e. free ends, constrained ends and full constraint. For the free-ends condition, there is no additional longitudinal constraint imposed on the two end-surfaces of the shortened wall component; for the constrained-ends condition, the longitudinal displacements of the nodes on the two end-surfaces corresponding to the start and stop boundaries are constrained; for the full-constraint condition, all the nodes in the meshed wall component are constrained from longitudinal motion.

In the long mechanical model, all dimensions were set to be the same as those in the previous experiments [20, 23], and elasto-plastic properties identical to the short model were used. The

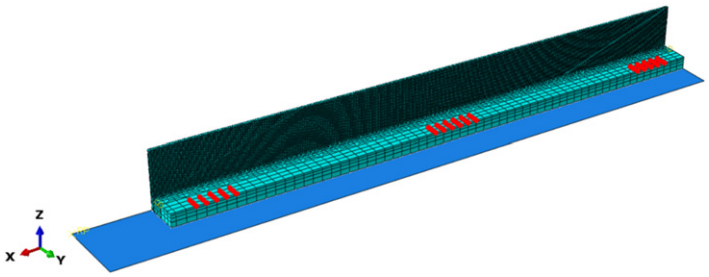


Figure 3. Mapped long mechanical model to simulate the removal of clamps (the constrained nodes representing the clamps are indicated in red).

steady-state PS and RS that were predicted by the short model were mapped to the long model using the solution mapping technique (section 2.2). In addition, the longitudinal constraint used in the short model was removed in the long model. The backing-plate support to the built component was simulated through surface-to-surface contact interaction between the substrate bottom and an analytic rigid shell. The clamps were simulated through fixing the selected nodes on the top surface of the substrate (figure 3). During the mechanical analysis using the long model, stress balancing was first established and then the clamps were removed to obtain the final state. To eliminate the potential rigid body motion of the WAAM component, the symmetry boundary condition and the contact interaction remained after clamps removal; in addition, one node was fully fixed on the central bottom in the symmetry plane.

2.4. Rolling model and verification method

The efficient modelling approach (sections 2.1 and 2.2) was also applied to high pressure rolling on a wall component with identical geometry to the WAAM component, as shown in figure 4. The rolling simulation considered two scenarios. In the first scenario, the rolling was performed on the component with a stress-free initial condition, i.e. pure rolling analysis. In the second scenario, the WAAM and rolling processes were combined, and the WAAM-induced PS and RS were defined as the initial condition for the rolling simulation.

The setup of the short rolling model was detailed in a previous paper by the same authors [39]. Only key information is repeated here for brevity. The temperature was assumed to be room temperature and kept constant when the rolling was simulated as an individual process. When rolling was combined with WAAM, the rolling was performed on the top surface of the WAAM deposited wall after cooling, i.e. post-build rolling simulation (inter-layer rolling simulation will be reported separately in another paper). The flat roller was modelled as a rigid shell. The assumption of rigid roller is beneficial to computational efficiency without impairing solution accuracy [39]. For pure rolling simulation, the substrate and wall were modelled as a deformable body with material properties adopted from reference [31] for mild steel S355. A vertical rolling load of 50 kN was imposed to the wall through controlling the penetration displacement of the roller and a friction coefficient of 0.3 was assumed for the contact between the roller surface and the top surface of the wall. All nodes on the bottom surface of the substrate were fixed to represent the clamps during rolling. Similar to the short WAAM model, different longitudinal constraint conditions (i.e. free ends, constrained ends and full constraint) were considered in the short rolling model to investigate the sensitivity of the predicted results to the assumed longitudinal constraint.

To verify the efficacy of the short model, a conventional full-size transient rolling model (500 mm long) was also developed [39]. The PS and RS distributions predicted by the short

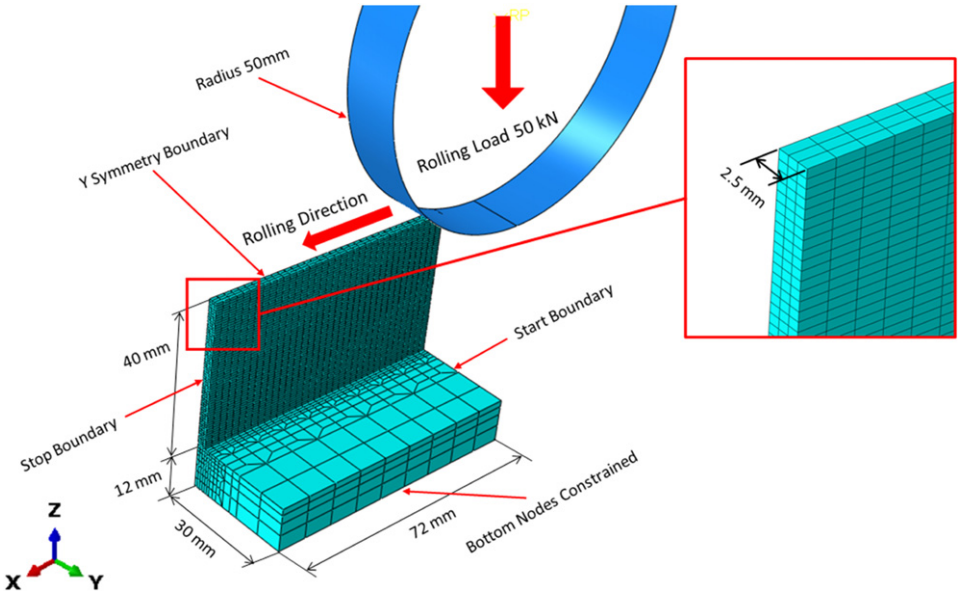


Figure 4. Short rolling model for a wall component with identical geometry to the WAAM component (figure 2). Adapted from [39]. CC BY 4.0.

model were compared with those predicted by the full-size model for the steady state of rolling, such that the accuracy of the short model to predict steady-state PS and RS can be verified.

Finally, the steady-state solution of the short model was also transferred to a long mechanical model using the solution mapping technique (section 2.2), similar to the WAAM model (figure 3). The mapped long model was then employed for the analysis of RS and distortion in the rolled wall after removal of clamps.

2.5. WAAM + rolling model

A sequential coupling approach was used to model the combination of WAAM and rolling. The solution to the mechanical model of the WAAM deposition was used as the initial condition for the rolling model. The solution mapping technique (section 2.2) was used to define the initial condition for the post-build rolling simulation. The WAAM + rolling model is aimed to reveal the mechanism of the rolling-enabled mitigation of the RS and distortion in the WAAM deposited wall component. The combination of WAAM and rolling was simulated for the identical wall component modelled in sections 2.3 and 2.4.

3. Results and discussion

3.1. Computational efficiency

The computational efficiency of the developed modelling approach is evaluated through comparison of computational time between the efficient model and conventional full-size model. The WAAM and rolling simulations were implemented using four processors in a grid computer system at Cranfield University. Table 1 presents the comparison between the conventional full-size transient WAAM model developed by Ding *et al* [20] and the efficient WAAM model developed in this study. Using the efficient model, the computational

Table 1. Computational time comparison between the conventional full-size WAAM model [20] and the efficient WAAM model developed in this study.

	Computational time of thermal model for WAAM	Computational time of mechanical model for WAAM	Total computational time
Conventional full-size WAAM model [20]	51 h, 24 min	24 h, 1 min	75 h, 25 min
Efficient WAAM model	12 h, 18 min	26 min-short model 5 min-long model	12 h, 49 min
Time saving	76.1%	97.8%	83.0%

Table 2. Computational time comparison between the conventional full-size rolling model [39] and the efficient rolling model developed in this study.

	Computational time for rolling simulation	Computational time of mapped long mechanical model	Total computational time
Conventional full-size rolling model [39]	17 h, 47 min	N/A	17 h, 47 min
Efficient rolling model	37 min [39] (short model)	7 min	44 min
Time saving	96.5%	N/A	95.9%

time can be reduced by 76.1% and 97.8% for thermal and mechanical analyses, respectively, and an 83% reduction in total computational time was achieved. For rolling simulation, 95.9% less computational time was consumed by the efficient model in comparison with the conventional full-size model (table 2). Therefore, it can be concluded that the developed modelling approach can significantly enhance the efficiency of both WAAM and rolling simulations.

The saving of the computational time is mainly attributed to the reduction of the number of elements in the model and the less process time involved in the simulation. The short model consists of approximately 9000 elements, while the number of elements is approximately 63 000 for the conventional full-size model. As the short models considered only 14.4% length of the actual component, it means that the travel time of the heat source or roller over the component length in the short models is only 14.4% of the travel time for the full-size component. Unlike the conventional full-size transient model, the mapped long mechanical model used here took only several minutes to obtain the solution, because it did not simulate the WAAM and rolling processes but instead mainly calculated the RS and distortion after removal of clamps, which was much less computationally expensive. The reduction in computational time using the efficient method does not sacrifice the solution accuracy, which will be elaborated in following sections.

3.2. WAAM deposition

3.2.1. Thermal analysis using short model. The accuracy of the thermal solution obtained by the short WAAM model is verified through comparing the predicted transient temperatures with the experimental measurements using thermocouples [23]. The locations of the thermocouples (TP1–TP4) used in the experiments are shown in the cross-section of the WAAM thermal model (figure 2). Figure 5 shows the comparison of the temperature histories at the

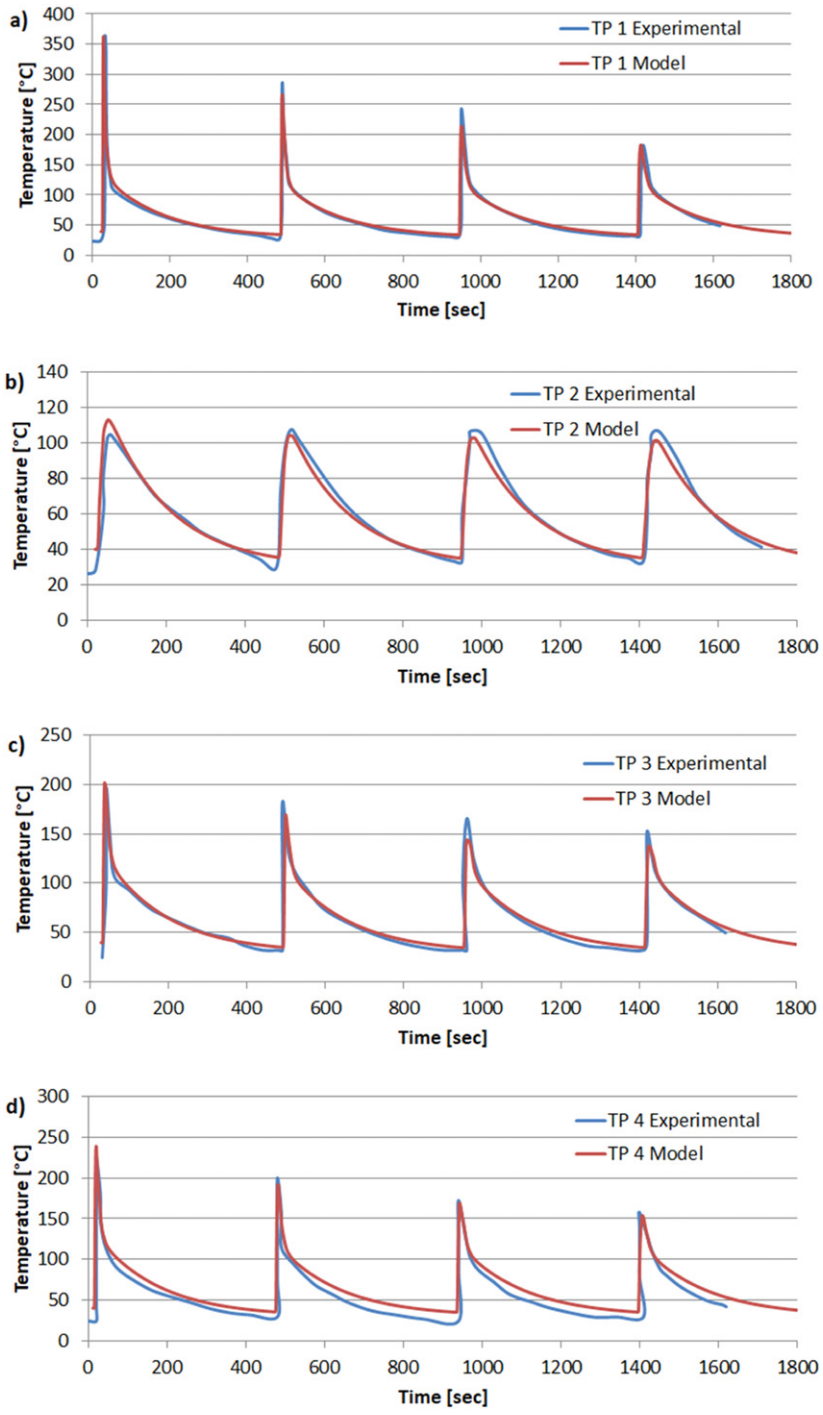


Figure 5. Temperature histories predicted by the short WAAM thermal model at the thermocouple locations: (a) TP1, (b) TP2, (c) TP3 and (d) TP4. The experimental measurements by Ding [23] are also included for comparison.

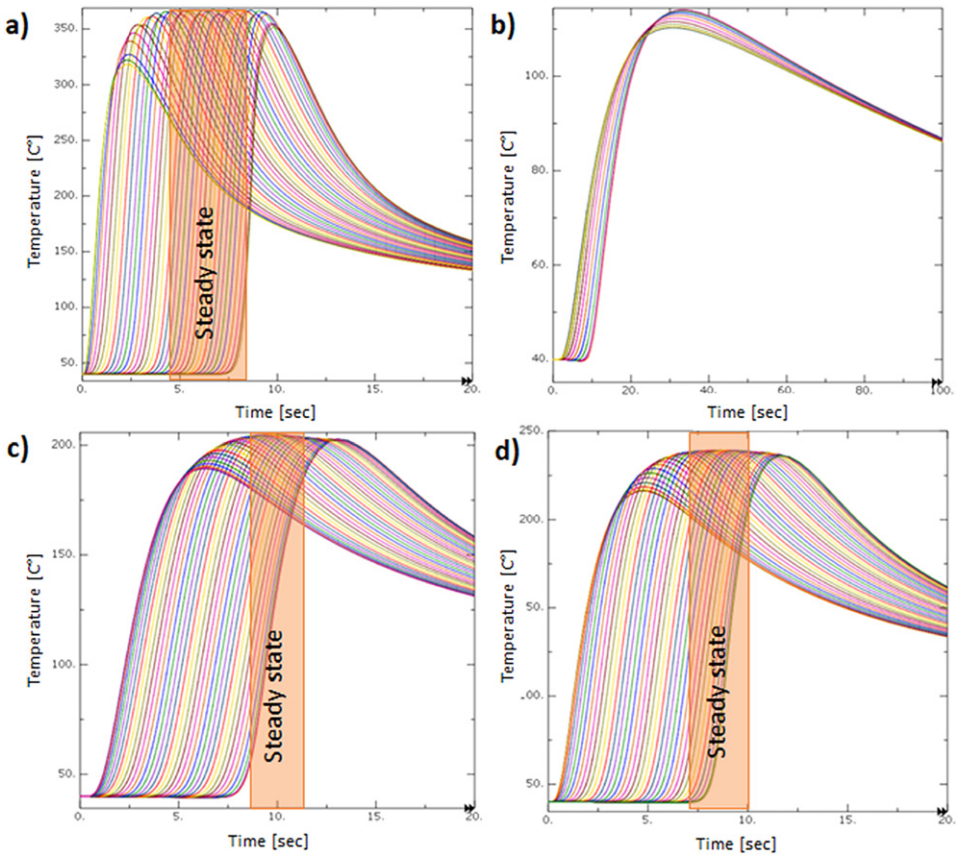


Figure 6. Predicted temperature histories at different longitudinal locations (i.e. different X coordinates) which are coincident with (a) TP1, (b) TP2, (c) TP3 and (d) TP4 in the YZ plane (see figure 2 for locations of TP1–TP4). Note that the peak temperatures corresponding to steady state of the WAAM deposition are highlighted.

thermocouple locations for the first four layers. It should be noted that in the model the TP2 point is not located at any element node, so the interpolated temperature is used. Good agreement between the prediction and measurement is evident, verifying the accuracy of the thermal solution by the short model.

To identify the steady-state region for the temperature field during WAAM deposition, the temperature histories at different longitudinal locations are compared in figure 6. These inspected locations share the Y and Z coordinates with the thermocouple locations (TP1–TP4), but have different X coordinates. We denote these locations using the thermocouple labels (TP1–TP4). The longitudinal location closest to the WAAM start boundary experienced temperature rise first, but its peak temperature is lowest. The highest peak temperature was attained at the locations where the temperature started to rise after 2.5–3.5 s, corresponding to a distance of 21–29 mm to the WAAM start boundary. For the TP1, TP3 and TP4 locations, the highest peak temperatures are constant within a period of time, indicating the time-independence of the peak temperature and the attainment of the steady state. In other words, the temperature histories in the steady-state region are independent of X coordinates in the longitudinal direction. For the TP2 locations in the substrate far from the deposited wall (fewer data are available due

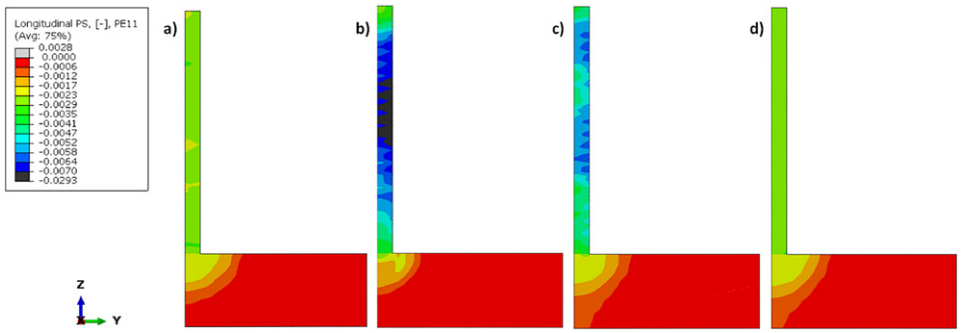


Figure 7. Cross-sectional distributions of longitudinal PS in the steady-state region for the WAAM: (a) full-size mechanical model [23]; (b) short mechanical model with free ends; (c) short mechanical model with constrained ends; (d) short mechanical model with full longitudinal constraint.

to the coarse mesh adopted at theses locations, see figure 2), the heating and cooling are much slower, and a constant peak temperature cannot be conclusively distinguished. However, the far-field temperatures with low peaks do not contribute to the generation of RS after cooling [21]. The temperature results confirmed that the steady-state solution of near-field temperatures, which are critical to the RS development during WAAM deposition [21], can be obtained using the short thermal model.

3.2.2. Mechanical analysis using short model. The PS and RS distributions in the clamped WAAM component are analysed using the short mechanical model. The net thermal deformation after WAAM deposition is negligible since the temperatures in the initial, inter-layer and final states are all approximately same as room temperature (figure 5). Therefore, the process-induced PS is the main cause of the RS and hence it is important to accurately predict the PS. It should be also mentioned that the longitudinal PS and RS are focused here since they are most significant.

Figure 7 shows the predicted longitudinal PS distributions in the steady-state region after the deposition of the 20 layers. The results for different longitudinal constraint conditions adopted in the short model are compared. The prediction by the full-size mechanical model [23] is used as a reference to evaluate the accuracy of the steady-state solution of the short model. The PS is compressive and approximately uniform (ranging from -0.2% to -0.3%) in the deposited wall. The substrate region immediately underneath the wall experienced less plastic deformation, ranging from -0.06% to -0.2%, while the substrate region far from the wall did not experience any plastic deformation. The short model with full longitudinal constraint best captured the PS profiles, while the short models with free ends and constrained ends overestimated the compressive PS in the wall, and it appears that the less the longitudinal constraint, the more significant the overestimate.

Figure 8 shows the 3D distributions of the PS predicted by the full-size model [23] and the short model with full longitudinal constraint. According to the full-size model, the predicted PS distribution is approximately uniform over the majority of the interior region of the long wall (i.e. steady-state region), except some slight deviation near the clamps (three clamps on each side of the substrate, see figure 3). However, the compressive PS near the wall ends (free from longitudinal constraint in the full-size model) are significantly higher than that in the steady-state region, and this feature is consistent with the effect of longitudinal constraint on PS, as revealed by the

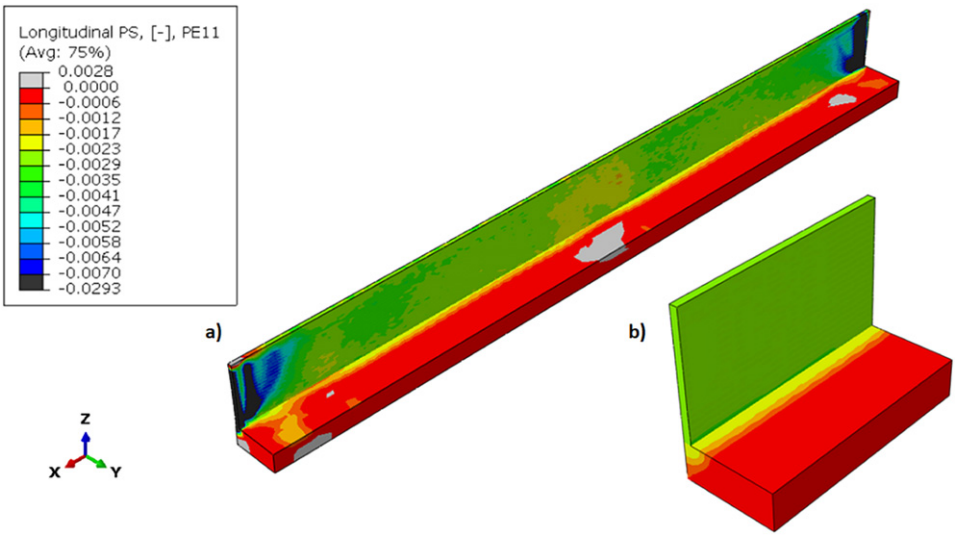


Figure 8. 3D distributions of the longitudinal PS for the WAAM: (a) full-size mechanical model [23]; (b) short mechanical model with full longitudinal constraint.

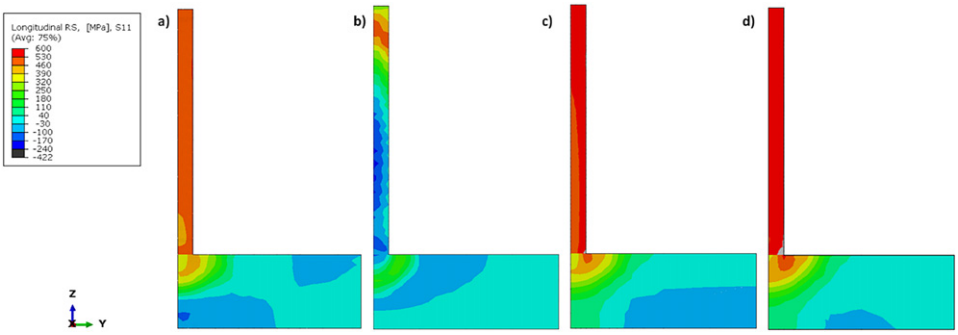


Figure 9. Cross-sectional distributions of longitudinal RS in the steady-state region for the WAAM: (a) full-size mechanical model [23]; (b) short mechanical model with free ends; (c) short mechanical model with constrained ends; (d) short mechanical model with full longitudinal constraint.

short model (figures 7(b) and (c)). In contrast, the short model with full longitudinal constraint completely avoided the wall end effect and thus is reliable to obtain the steady-state solution. It is also seen that there is a slight discrepancy of predicted PS level in the middle of the wall between the full-size model and short model. This discrepancy can be attributed to the difference in the application of clamps in the models, i.e. in the full-size model [23], the nodal displacements were restrained at the three clamps locations similar to those shown in figure 3, while in the short model, the actual clamp locations cannot be represented due to the reduced component length and only two clamps were considered (figure 2).

Figure 9 shows the predicted longitudinal RS distributions in the steady-state region. The full-size model [23] predicted tensile RS in both the wall and the substrate region immediately below the wall (figure 9(a)), while counterbalancing compressive longitudinal RS formed in the lower and side regions of the substrate. The RS distribution predicted by the short model

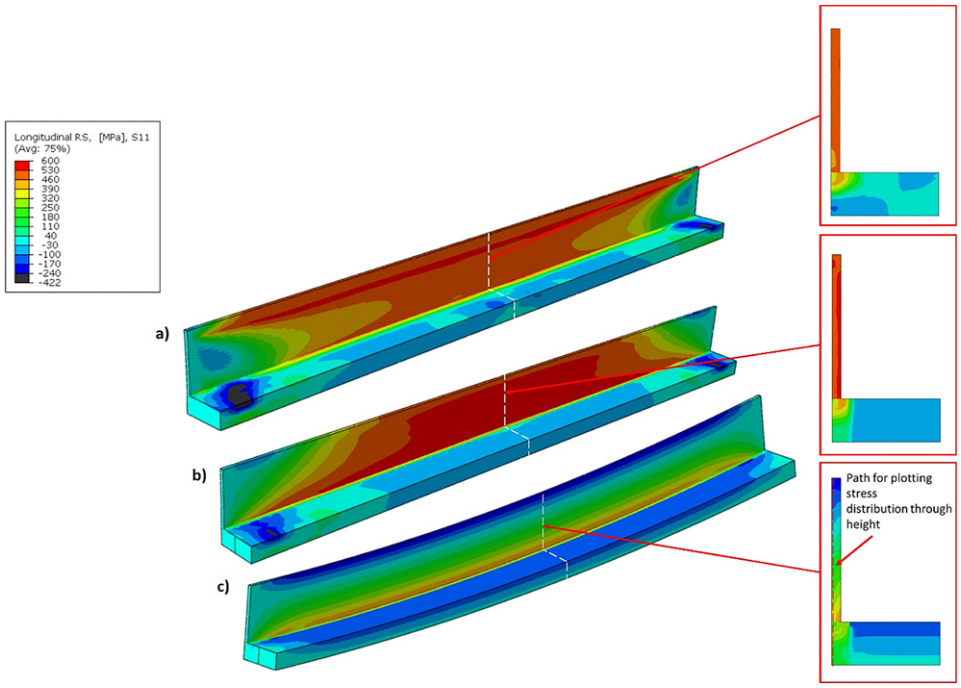


Figure 10. Longitudinal RS distributions predicted by the long mechanical models for the WAAM: (a) conventional full-size model under clamped condition [23]; (b) mapped model under clamped condition; (c) mapped model after clamps removal (a deformation scale factor of 5 is used to improve visibility of distortion). The RS distributions in the middle-length section are also shown.

with free ends (figure 9(b)) is markedly different from that predicted by the full-size model (figure 9(a)), mainly due to the large difference in PS distribution (figures 7(a) and (b)). The RS predictions by the short models with constrained ends and full longitudinal constraint, as shown in figures 9(c) and (d), respectively, are both similar to the prediction by the full-size model (figure 9(a)), although the short model with constrained ends overestimated the PS in the wall (figure 7(c)).

3.2.3. Mechanical analysis using mapped long model. The steady-state solution of the short mechanical model with full longitudinal constraint was mapped to the long mechanical model. The comparison between the conventional full-size model and mapped long model, as shown in figures 10(a) and (b), confirms that the steady-state solution is equivalent between the two models. The efficacy of the mapping (sections 2.1–2.3) is demonstrated through comparison between figures 9(d) and 10(b), which show that the longitudinal RS distributions in the steady-state region are similar between the short model (donor) and the long model (recipient). The slight discrepancy in steady-state RS can be attributed to the limitation of the solution mapping technique (section 2.2) and the differences in the longitudinal constraint condition and clamps locations between the short and long models (figures 2 and 3). The mapped long model also captured the nonuniform RS distributions near the two free ends of the full-size component, while the short model lacks this capability.

After removal of clamps, the tensile RS in the wall reduces significantly and even converts to compression on the top surface of the wall (figure 10(c)). Concave upward bending distortion

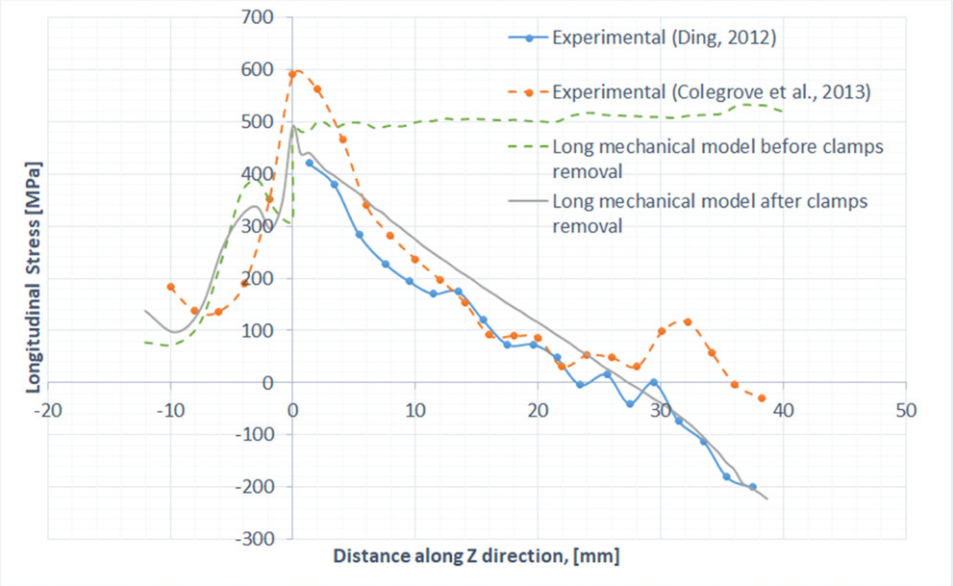


Figure 11. Longitudinal RS distributions along the *Z*-direction (with distance from the upper surface of the substrate, see figure 10(c) for the path of the line plots) in the mapped long mechanical model before and after clamps removal for the WAAM component. The experimental measurements by Ding [23] and Colegrove *et al* [5] are also included, which were conducted using neutron diffraction method after clamps removal.

was generated due to the partial relaxation of the original tensile RS in the wall, and the material response to the removal of clamps was essentially elastic as no additional PS was generated. It should be mentioned that additional simulation of removal of clamps using the short model was also conducted and it was found that the short model was not able to capture the bending distortion, indicative of the necessity of the mapped long model.

Figure 11 presents the through-height line profiles of the longitudinal RS distribution in the steady-state region. Under the clamped condition, the mapped long model predicted uniform tensile RS of 500 MPa in the whole wall, which rapidly reduces to 300 MPa in the substrate, since the substrate has lower yield strength, larger cross-sectional area and smaller compressive PS (figure 7). The tensile RS in the wall dropped significantly after removal of clamps, and the final RS exhibits an approximately linear distribution. The RS prediction and measurements agree well, indicative of good accuracy of the mapped long mechanical model.

In order to further assess the solution accuracy, the predicted distortion after clamps removal was compared to the experimental measurement [23] for a four-layer WAAM deposited wall (figure 12). Good agreement between the prediction and measurement is evident, and the small discrepancy could be attributed to the idealisation of the clamps (nodal displacements are fixed at clamping locations in the model, while the clamps may not be fully rigid in the experiment).

3.3. High pressure rolling

3.3.1. Mechanical analysis using short model. Pure rolling analysis is presented in this section. The PS and RS distributions predicted by the short rolling model for the clamped wall component have been reported in a previous paper by the same authors [39]. Here, the analysis is focussed on the effects of different longitudinal constraint conditions on the results,

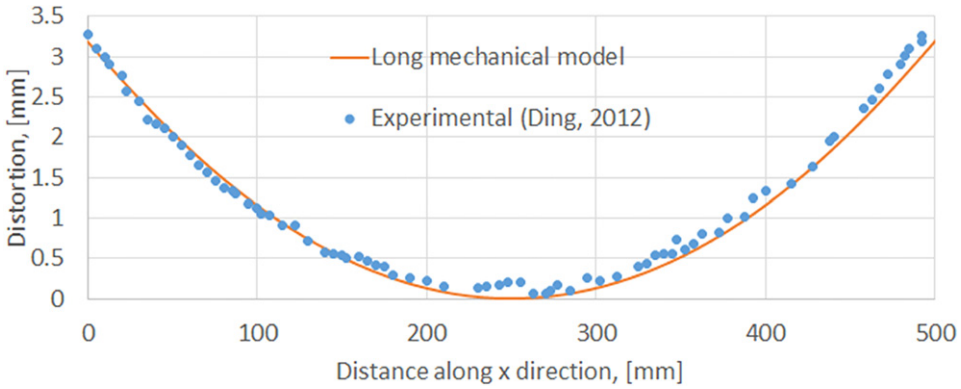


Figure 12. Validation of out-of-plane distortion prediction by the mapped long mechanical model after clamps removal. Note that the experimental measurement by Ding [23] was based on a four-layer deposited wall, and the WAAM model was adapted accordingly. The distortion measurement was conducted on the substrate bottom using a Romer omega arm with R-scan 3D laser scanning system [23].

as well as the RS redistribution due to removal of clamps. It should be noted that the steady state of rolling is identified in the region where the equivalent PS is uniformly distributed in the longitudinal direction and it has been confirmed that the short model has captured the steady state [39].

Figure 13 shows the longitudinal PS distributions in the steady-state region of the rolled wall. The wall height was reduced after the rolling by the flat roller with the vertical load of 50 kN, and the height reduction was 1.668 mm. The wall region near the roller expanded laterally. It is clearly seen that the longitudinal constraint has pronounced effect on the PS results. The conventional full-size model predicted tensile PS near the rolled top surface. The short model with constrained ends predicted most accurate PS distribution relative to the solution by the full-size model, while the short model with free ends overestimated the PS and the short model with full longitudinal constraint underestimated the PS. The PS has significant implication in the RS generated after rolling, as revealed below.

Figure 14 shows the longitudinal RS distributions in the steady-state region of the rolled wall. In consistence with the PS distributions, the solution of the short model with constrained ends achieved best agreement with the solution of the full-size model. The RS is tensile underneath the rolled surface, and it is compressive underneath the tension zone and near the wall side. Both the short models with free ends and full longitudinal constraint underestimated the RS.

3.3.2. Mechanical analysis using mapped long model. Figure 15 shows the longitudinal RS distributions predicted by the long mechanical models for the rolling. It is evident that equivalent steady-state solution was obtained by the conventional full-size model and the mapped long model (figures 15(a) and (b)). The RS distribution in the steady-state region is almost unchanged after the solution mapping from the short model with constrained ends (figures 14(c) and 15(b)). The removal of clamps results in expansion of tension zone underneath the rolled surface and shrinkage of compression zone underneath the tension zone. However, the effect of clamps removal on the overall RS distribution in the rolled wall is marginal (figure 15), unlike the significant effect for the WAAM (figure 10). Moreover, no discernible bending distortion

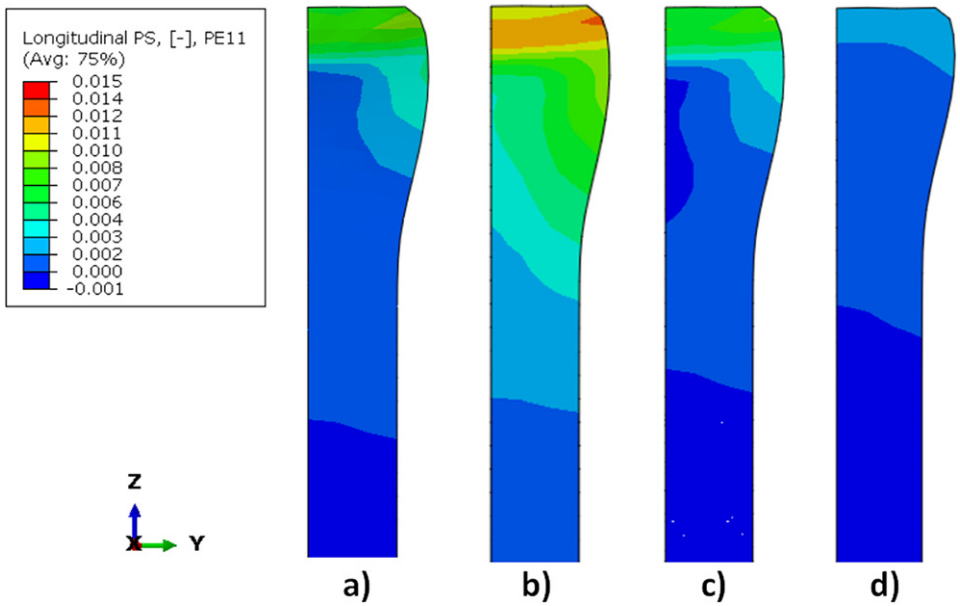


Figure 13. Comparison of predicted longitudinal PS distributions in the steady-state region of high pressure rolling: (a) conventional full-size model [39]; (b) short model with free ends; (c) short model with constrained ends [39]; (d) short model with full longitudinal constraint.

of the rolled wall was generated after clamps removal (figure 15(b)). The reason for the unapparent distortion after rolling is twofold. First, the rolling RS in the clamped condition did not generate significant bending moment; this can be verified by inspecting the reaction forces at the clamp locations in the model. The total vertical force for the three clamps (figure 3) was compressive, and it was 5002 N for the rolling model, approximately one-order lower than that (53 118 N) for the WAAM model. Second, since the clamp forces were small in the rolling model, after the removal of clamps there was little relaxation of RS and hence the rolled wall did not experience apparent distortion, in contrast to the significant bending distortion in the WAAM model (figure 10).

3.4. Combination of WAAM and rolling

The results of the WAAM + rolling model are presented in this section. For the modelling of the combined process, full longitudinal constraint was used for the WAAM deposition, while longitudinal constraint on the two ends was used for the rolling. The change in the constraint barely affects the modelling results for two reasons. First, the plastic deformation was permanent, and the PS predicted by the WAAM model did not change after the partial relaxation of the constraint in the rolling model. Second, the WAAM-generated RS is similar between the full constraint model and the end constraint model (figures 9(c) and (d)), meaning that the initial stress condition in the rolling model after WAAM deposition was insensitive to the change in the longitudinal constraint.

Figure 16 shows the longitudinal PS distributions in the steady-state region. After WAAM deposition, compressive PS is dominant in the wall (figure 16(a)). The rolling gave rise to tensile PS, and hence the compressive PS caused by WAAM deposition was reduced after

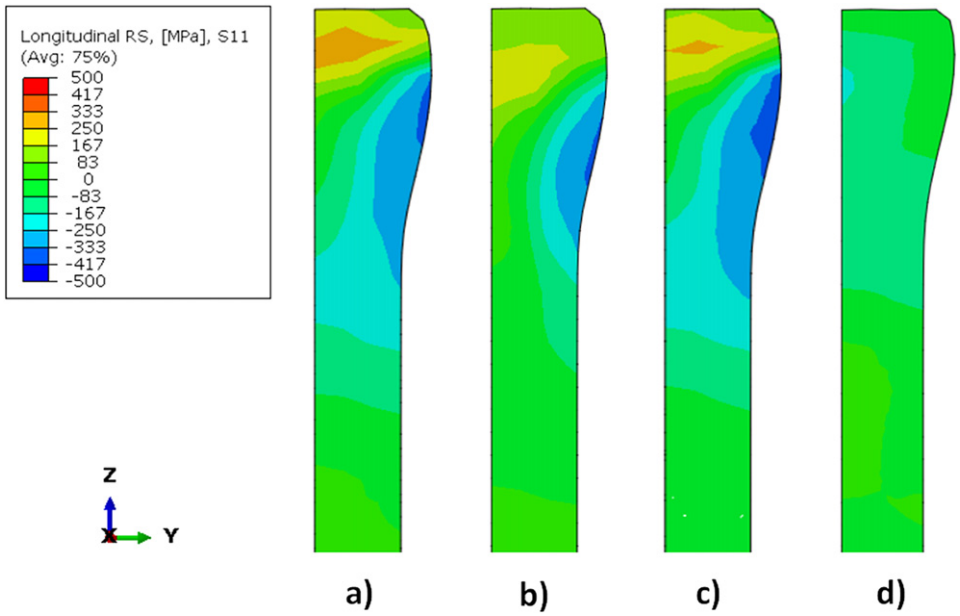


Figure 14. Comparison of predicted longitudinal RS distributions in the steady-state region of high pressure rolling: (a) conventional full-size model; (b) short model with free ends; (c) short model with constrained ends; (d) short model with full longitudinal constraint. Adapted from [39]. CC BY 4.0.

rolling (figure 16(b)). Given the 50 kN rolling load used, significant tensile PS was generated near the rolled surface (figure 16(b)), which is similar to the tensile PS in the pure rolling model (figure 13(c)). This means that the PS induced by the rolling overwhelms the PS induced by the WAAM deposition near the rolled surface. However, when the rolling load is reduced, it is anticipated that the rolling-induced PS will also decrease and then it will have less impact on the WAAM-induced PS. It is interesting to see that the removal of clamps does not affect the PS distribution, indicative of the elastic nature of the material response (figures 16(c) and (d)).

Figure 17 shows the longitudinal RS distributions in the steady-state region. It is clearly seen from figures 17(a) and (b) that the post-build rolling reduces the tensile RS in the WAAM-deposited wall, while the RS in the substrate is less affected, due to the large distance from the substrate to the rolled surface. The mitigation of WAAM deposition RS through rolling can be attributed to the effect of rolling on PS, i.e. rolling introduces tensile PS and reduces the compressive PS in the WAAM-deposited wall (figure 17). Interestingly, the RS in the wall is similar between the combined WAAM-rolling model (figure 17(c) and (d)) and the pure rolling model (figure 15). This means that the rolling dominates the final RS in the wall for the given rolling load of 50 kN (figure 4). Abbaszadeh *et al* [40] also found that at large rolling loads (>20 kN) the rolling models with and without the initial RS condition associated with WAAM deposition predicted similar longitudinal RS distributions in the rolled wall. Finally, the removal of clamps results in slight decrease of tensile RS in both the wall and substrate (figure 17(d)).

Figure 18 shows the 3D distributions of the longitudinal RS in the wall component, which are similar between the clamped and unclamped conditions. In addition, there is no considerable distortion found after removal of clamps. This is because the WAAM deposition RS in

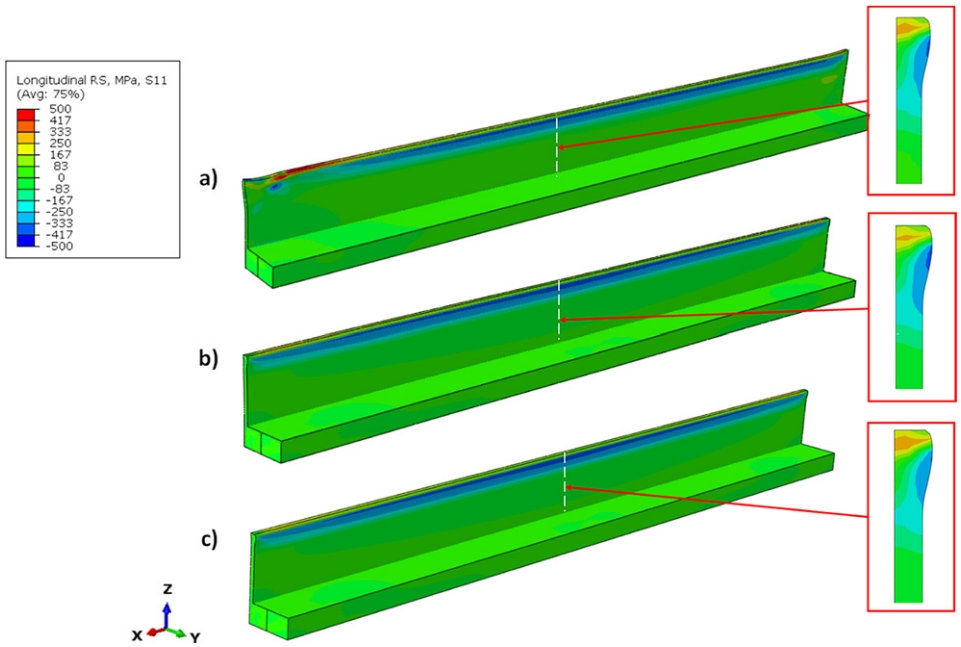


Figure 15. Longitudinal RS distributions predicted by the long mechanical model for the high pressure rolling: (a) conventional full-size model under clamped condition [39]; (b) mapped model under clamped condition; (c) mapped model after clamps removal (a deformation scale factor of 5 is used to improve visibility of distortion). The RS distributions in the middle-length section are also shown.

the clamped condition has been largely mitigated by rolling and then no much RS was relaxed during clamps removal to generate distortion.

3.5. Generalisation and limitation

This study has demonstrated that the developed modelling approach (sections 2.1 and 2.2) is efficient to simulate both WAAM and rolling (sections 3.1–3.4), which enables analyses and understanding of individual WAAM/rolling and combined WAAM + rolling processes for large components encountered in practice, as presented and discussed in sections 3.1–3.4. This efficient modelling approach could also be applied to other manufacturing processes (e.g. welding and machining), as long as steady state exists.

There are three key considerations in this efficient modelling approach.

First, a proper length for the shortened component should be used in the short model. The attainment of steady state has been verified for both WAAM (figures 6, 7 and 8) and rolling [39]. The gain of higher efficiency through further reducing the model length is marginal. The advantage of the short 3D model over 2D model lies in the fact that the physical mechanisms involved in the manufacturing processes are essentially 3D and the short 3D model is able to capture these mechanisms but the 2D model is not. For instance, accurate prediction of transient temperature field during WAAM deposition relies on the modelling formulation of heat source and heat transfer, of which both exhibit 3D characteristics. It has been also demonstrated that a 2D rolling model has limited predictive capability and accuracy [39]. Nevertheless, a 2D mechanical model (e.g. plane strain model) could be used for the WAAM deposition based on

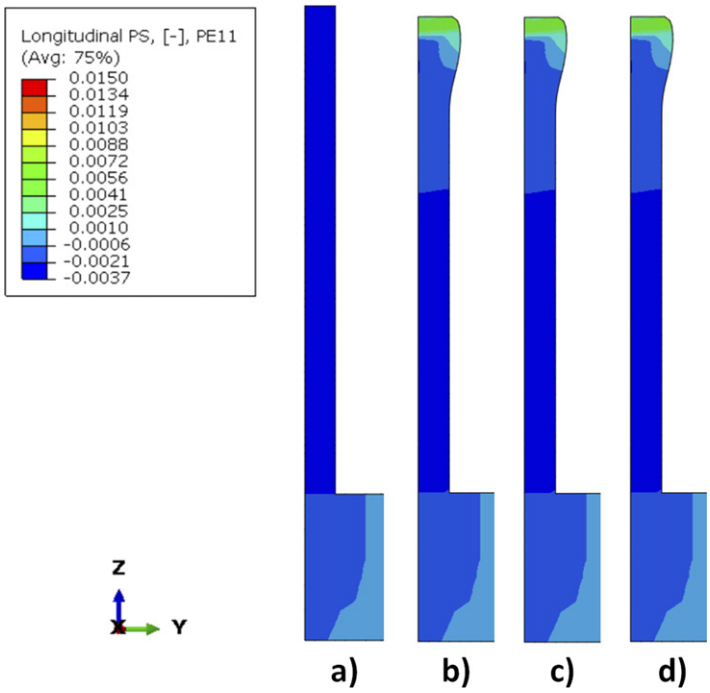


Figure 16. Predictions of longitudinal PS distributions in the steady-state region for the combined WAAM and rolling process: (a) short model with clamps before rolling; (b) short model with clamps after rolling; (c) mapped long model with clamps; (d) mapped long model after clamps removal.

the transient temperature field predicted by the short 3D thermal model. Such an attempt can potentially further reduce the computational time, although the short 3D mechanical model is already efficient (table 1). Given a full longitudinal constraint used in the short WAAM model, a plane strain condition assumed in a 2D mechanical model is valid in such a case, but the modelling can be complicated due to transferring solution between 3D thermal model and 2D mechanical model [47]. On the other hand, plane strain condition is not acceptable when WAAM is combined with rolling.

Second, proper longitudinal constraint should be imposed to the short mechanical model. It is interesting to see that, given identical component length, to obtain accurate steady-state solution, full longitudinal constraint is needed for the short WAAM model (figures 7 and 9), while longitudinal constraint is only needed on the two end-surfaces of the wall component for the short rolling model (figures 13 and 14). This difference can be attributed to the distinctive mechanisms for plastic flow during WAAM and rolling processes. For the studied WAAM process, the PS is generated primarily due to internal constraint of isotropic thermal deformation upon localised heating/cooling and it occurs mainly at high temperatures when the yield strength is low; a full longitudinal constraint does not change the deformation mode and is representative in the steady-state WAAM region for the studied long component. The constrained-ends condition does not provide sufficient longitudinal constraint in the steady-state region of the short WAAM model adopted here (figure 7(c)). However, if the actual length of the component (figure 3) is shorter, the additional longitudinal constraint needed in the short model could be lower. For the studied rolling process, the PS results from the vertical

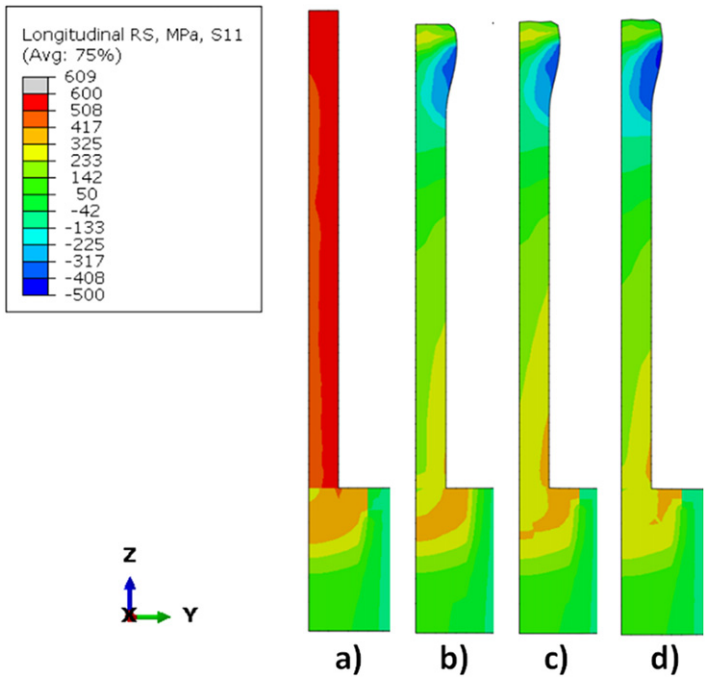


Figure 17. Predictions of longitudinal RS distributions in the steady-state region for the combined WAAM and rolling process: (a) short model with clamps before rolling; (b) short model with clamps after rolling; (c) mapped long model with clamps; (d) mapped long model after clamps removal.

penetration of roller at room temperature and assuming full longitudinal constraint adds unphysical resistance to the roller penetration and thus is not representative in the steady-state rolling region. Therefore, it is crucial to impose proper longitudinal constraint in the short model in order to obtain accurate steady-state solution, and the needed additional constraint being equivalent to that for the full length is dependent on specific processes and components that are modelled.

Third, a long mechanical model representative for the actual component geometry, with the steady-state solution mapped from the short model as initial condition, is needed for the analysis of final state after removal of clamps. However, the computational time for the mapped long model is much less than the conventional full-size WAAM or rolling model (tables 1 and 2), which is particularly beneficial to the computational efficiency. This benefit is realised because the computationally expensive WAAM and rolling simulations are conducted using the short model, while only the effects of clamps removal are analysed by the mapped long model.

The main drawbacks of the developed efficient modelling approach include: (1) the mapping of steady-state solution requires same geometric feature and mesh topology of the component along the longitudinal direction; (2) the mechanical response in the regions corresponding to the unsteady-state WAAM deposition or rolling at the two ends of the modelled component cannot be accurately captured. These drawbacks do not impair the accuracy of the steady-state solutions obtained by the WAAM and rolling models (sections 3.2 and 3.3).

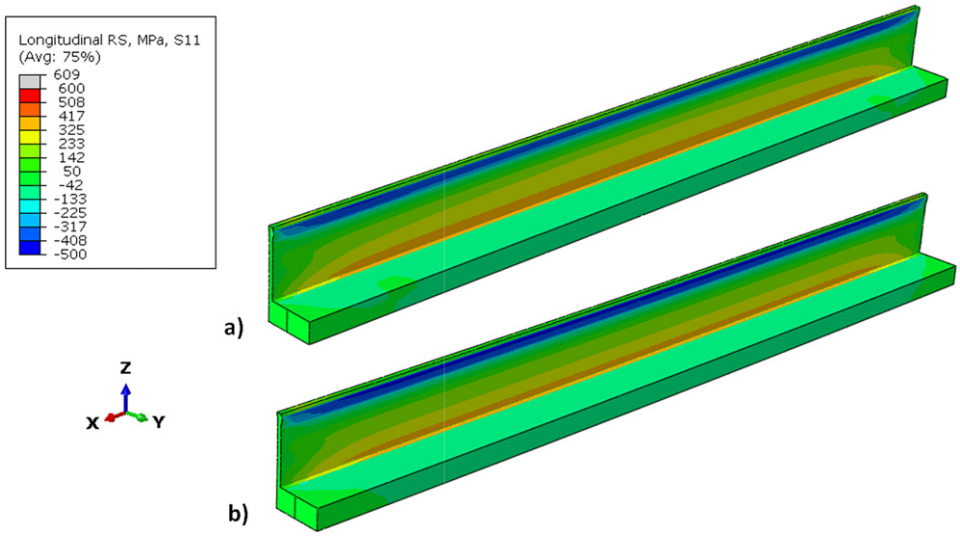


Figure 18. 3D distributions of longitudinal RS predicted by the mapped long mechanical model for the combined process of WAAM and rolling: (a) before clamps removal; (b) after clamps removal (a deformation scale factor of 5 is used to improve visibility of distortion).

Another limitation of the efficient modelling approach is that the short mechanical model is applicable to distortion prediction only when the component is clamped during the WAAM deposition and rolling. A full-size mechanical model is still needed to capture the in-process distortion when the component is not effectively clamped or intentionally allowed to move in certain directions. In such a case, the inherent strain method [35–37] can be used as an efficient solution to the in-process distortion simulation, which can also be used to handle complicated component geometry. Nevertheless, the short model can still be used to estimate the inherent strain for such an analysis.

4. Concluding remarks

An efficient modelling approach is developed to determine temperature, PS, RS and distortion in large-scale manufacturing. In this approach, a short model is used to obtain steady-state solution for a clamped component and then the solution is mapped to a long model for analysis of final RS and distortion after removal of clamps. This approach has been applied to simulate WAAM, rolling and their combination for a wall component, and it can potentially be used as a general method for other manufacturing processes, as long as steady state exists. The following conclusions are drawn:

(a) Computational time of WAAM and rolling simulations can be significantly reduced using the developed efficient modelling approach. The high efficiency is gained through reducing the component length and process time considered in the simulation to obtain steady-state solution. The enhanced efficiency is essential for simulation of large-scale WAAM + rolling process.

(b) The short models for WAAM and rolling can obtain steady-state solutions equivalent to those obtained by conventional full-size models, as long as proper additional constraint is

imposed. A full longitudinal constraint is needed in the short WAAM model for the studied wall component, while only the two ends of the shortened component need to be constrained in the short rolling model.

(c) For the WAAM deposition, the predictions of temperature, RS and distortion are in good agreement with experimental measurements. Within the steady-state region, approximately uniform compressive longitudinal PS is generated in the wall, which is responsible for the tensile longitudinal RS under the clamped condition. For the rolling process, tensile longitudinal PS is generated and concentrated near the top surface rolled by the flat roller, where both tensile and compressive longitudinal RSs arise. Unlike WAAM, after rolling the removal of clamps does not cause considerable distortion.

(d) For the combined WAAM + rolling process, the rolling can effectively mitigate the tensile RS in the WAAM-deposited wall under clamped condition, because the rolling introduces tensile PS that counteracts the compressive PS generated by the WAAM deposition. The rolling-enabled mitigation of RS in the clamped wall implies that, the WAAM bending distortion caused by the stress relief after clamps removal can be effectively alleviated by the rolling.

(e) The short mechanical model assumes that the component is fully clamped during WAAM deposition, and hence it cannot capture in-process distortion, which may occur if the component is not effectively clamped. Nevertheless, the steady-state solution could be used for other modelling methods (e.g. inherent strain method) to handle the complicated restraint and geometry, and the solution mapping technique enables the estimate of distortion due to removal of clamps in the long mechanical model.

Acknowledgments

Initial part of this research was guided and supported by Paul Colegrove. Part of this research was technically aided by Daniel Cozzolino, Filomeno Martina and Matyas Benke. The authors also gratefully acknowledge the support by WAAMMat and the funding by EPSRC Grant EP/R027218/1 for the programme of New Wire Additive Manufacturing (NEWAM).

Author contribution

Conceptualization: Valeriy Gornyakov, Yongle Sun, Jialuo Ding, Stewart Williams; methodology: Valeriy Gornyakov; software: Valeriy Gornyakov; investigation: Valeriy Gornyakov, Yongle Sun; writing—original draft preparation: Valeriy Gornyakov; writing—review and editing: Yongle Sun, Jialuo Ding; visualization: Valeriy Gornyakov; supervision: Jialuo Ding, Yongle Sun, Stewart Williams; project administration: Jialuo Ding, Stewart Williams.

Declaration of competing interest

The authors declare that they have no known competing financial interests or personal relationships that could have appeared to influence the work reported in this paper.

Data availability statement

Data underlying this study can be accessed through the Cranfield University repository at https://doi.org/10.17862/cranfield.rd.14832180.

ORCID iDs

Valeriy Gornyakov https://orcid.org/0000-0002-8676-126X
Yongle Sun https://orcid.org/0000-0002-8401-8069

References

[1] Williams S W, Martina F, Addison A C, Ding J, Pardal G and Colegrove P 2016 Wire + arc additive manufacturing *Mater. Sci. Technol.* **32** 641–7
[2] Ding D, Pan Z, Cuiuri D and Li H 2015 Wire-feed additive manufacturing of metal components: technologies, developments and future interests *Int. J. Adv. Manuf. Technol.* **81** 465–81
[3] Lockett H, Ding J, Williams S and Martina F 2017 Design for wire + arc additive manufacture: design rules and build orientation selection *J. Eng. Des.* **28** 568–98
[4] Martina F, Ding J, Williams S, Caballero A, Pardal G and Quintino L 2019 Tandem metal inert gas process for high productivity wire arc additive manufacturing in stainless steel *Addit. Manuf.* **25** 545–50
[5] Colegrove P A, Coules H E, Fairman J, Martina F, Kashoob T, Mamash H and Cozzolino L D 2013 Microstructure and residual stress improvement in wire and arc additively manufactured parts through high-pressure rolling *J. Mater. Process. Technol.* **213** 1782–91
[6] Martina F, Roy M J, Szost B A, Terzi S, Colegrove P A, Williams S W, Withers P J, Meyer J and Hofmann M 2016 Residual stress of as-deposited and rolled wire + arc additive manufacturing Ti–6Al–4V components *Mater. Sci. Technol.* **32** 1439–48
[7] Asala G, Khan A K, Andersson J and Ojo O A 2017 Microstructural analyses of ATI 718 plus® produced by wire–arc additive manufacturing process *Metall. Mater. Trans.* A **48** 4211–28
[8] Gu J, Ding J, Williams S W, Gu H, Ma P and Zhai Y 2016 The effect of inter-layer cold working and post-deposition heat treatment on porosity in additively manufactured aluminum alloys *J. Mater. Process. Technol.* **230** 26–34
[9] Marinelli G, Martina F, Ganguly S and Williams S 2019 Microstructure, hardness and mechanical properties of two different unalloyed tantalum wires deposited via wire + arc additive manufacture *Int. J. Refract. Met. Hard Mater.* **83** 104974
[10] Marinelli G, Martina F, Lewtas H, Hancock D, Mehraban S, Lavery N, Ganguly S and Williams S 2019 Microstructure and thermal properties of unalloyed tungsten deposited by wire + arc additive manufacture *J. Nucl. Mater.* **522** 45–53
[11] Marinelli G, Martina F, Lewtas H, Hancock D, Ganguly S and Williams S 2019 Functionally graded structures of refractory metals by wire arc additive manufacturing *Sci. Technol. Weld. Join.* **24** 495–503
[12] Clark D, Bache M R and Whittaker M T 2008 Shaped metal deposition of a nickel alloy for aero engine applications *J. Mater. Process. Technol.* **203** 439–48
[13] Martina F, Colegrove P A, Williams S W and Meyer J 2015 Microstructure of interpass rolled wire + arc additive manufacturing Ti–6Al–4V components *Metall. Mater. Trans.* A **46** 6103–18
[14] Colegrove P A, Donoghue J, Martina F, Gu J, Prangnell P and Hönnige J 2017 Application of bulk deformation methods for microstructural and material property improvement and residual stress and distortion control in additively manufactured components *Scr. Mater.* **135** 111–8
[15] Martina F 2014 Investigation of methods to manipulate geometry, microstructure and mechanical properties in titanium large scale wire + arc additive manufacturing *PhD Thesis* Cranfield University
[16] Cordiano H V 1970 Effect of residual stresses on the low cycle fatigue life of large scale weldments in high strength steel *J. Eng. Ind.* **92** 86–92

[17] Webster G A and Ezeilo A N 2001 Residual stress distributions and their influence on fatigue lifetimes *Int. J. Fatigue* **23** 375–83
[18] Dong P and Brust F W 2000 Welding residual stresses and effects on fracture in pressure vessel and piping components: a millennium review and beyond *J. Press. Vessel Technol.* **122** 329–38
[19] Dong P 2005 Residual stresses and distortions in welded structures: a perspective for engineering applications *Sci. Technol. Weld. Join.* **10** 389–98
[20] Ding J, Colegrove P, Mehnen J, Ganguly S, Sequeira Almeida P M, Wang F and Williams S 2011 Thermo-mechanical analysis of wire and arc additive layer manufacturing process on large multi-layer parts *Comput. Mater. Sci.* **50** 3315
[21] Ding J, Colegrove P, Mehnen J, Williams S, Wang F and Almeida P S 2014 A computationally efficient finite element model of wire and arc additive manufacture *Int. J. Adv. Manuf. Technol.* **70** 227–36
[22] Zhao H, Zhang G, Yin Z and Wu L 2011 A 3D dynamic analysis of thermal behavior during single-pass multi-layer weld-based rapid prototyping *J. Mater. Process. Technol.* **211** 488–95
[23] Ding J 2012 Thermo-mechanical analysis of wire and arc additive manufacturing process *PhD Thesis* Cranfield University
[24] Montevecchi F, Venturini G, Scippa A and Campatelli G 2016 Finite element modelling of wire–arc-additive-manufacturing process *Procedia CIRP* **55** 109–14
[25] Montevecchi F, Venturini G, Grossi N, Scippa A and Campatelli G 2017 Finite element mesh coarsening for effective distortion prediction in wire arc additive manufacturing *Addit. Manuf.* **18** 145–55
[26] Xiong J, Lei Y and Li R 2017 Finite element analysis and experimental validation of thermal behavior for thin-walled parts in GMAW-based additive manufacturing with various substrate preheating temperatures *Appl. Therm. Eng.* **126** 43–52
[27] Graf M, Hälsig A, Höfer K, Awiszus B and Mayr P 2018 Thermo-mechanical modelling of wire–arc additive manufacturing (WAAM) of semi-finished products *Metals* **8** 1009
[28] Camilleri D, Comlekci T and Gray T G F 2005 Computational prediction of out-of-plane welding distortion and experimental investigation *J. Strain Anal. Eng. Des.* **40** 161–76
[29] Zhang L and Michaleris P 2004 Investigation of Lagrangian and Eulerian finite element methods for modeling the laser forming process *Finite Elem. Anal. Des.* **40** 383–405
[30] Shanghvi J Y and Michaleris P 2002 Thermo-elasto-plastic finite element analysis of quasi-state processes in Eulerian reference frames *Int. J. Numer. Methods Eng.* **53** 1533–56
[31] Michaleris P and DeBiccari A 1997 Prediction of welding distortion *Welding Journal* **76** 172–81
[32] Michaleris P, Zhang L, Bhide S R and Marugabandhu P 2006 Evaluation of 2D, 3D and applied plastic strain methods for predicting buckling welding distortion and residual stress. *Sci. Technol. Weld. Join.* **11** 707–16
[33] Ueda Y and Murakawa H 1985 Applications of computer and numerical analysis techniques in welding research *Mater. Des.* **6** 103–11
[34] Ueda Y, Kim Y C and Yuan M G 1988 A predicting method of welding residual stress using source of residual stress *Q. J. Japan Weld. Soc.* **6** 59–64
[35] Chen Q, Liang X, Hayduke D, Liu J, Cheng L, Oskin J, Whitmore R and To A C 2019 An inherent strain based multiscale modeling framework for simulating part-scale residual deformation for direct metal laser sintering *Addit. Manuf.* **28** 406–18
[36] Bugatti M and Semeraro Q 2018 Limitations of the inherent strain method in simulating powder bed fusion processes *Addit. Manuf.* **23** 329–46
[37] Liang X, Chen Q, Cheng L, Hayduke D and To A C 2019 Modified inherent strain method for efficient prediction of residual deformation in direct metal laser sintered components *Comput. Mech.* **64** 1719–33
[38] Cozzolino L D, Coules H E, Colegrove P A and Wen S 2017 Investigation of post-weld rolling methods to reduce residual stress and distortion *J. Mater. Process. Technol.* **247** 243–56
[39] Gornyakov V, Sun Y, Ding J and Williams S 2021 Computationally efficient models of high pressure rolling for wire arc additively manufactured components *Appl. Sci.* **11** 402
[40] Abbaszadeh M, Hönnige J R, Martina F, Neto L, Kashaev N, Colegrove P, Williams S and Klusemann B 2019 Numerical investigation of the effect of rolling on the localized stress and strain induction for wire + arc additive manufactured structures *J. Mater. Eng. Perform.* **28** 4931–42

[41] Tangestani R, Farrahi G H, Shishegar M, Aghchehkandi B P, Ganguly S and Mehmanparast A 2020 Effects of vertical and pinch rolling on residual stress distributions in wire and arc additively manufactured components *J. Mater. Eng. Perform.* **29** 2073–84
[42] Paudel B J, Marshall G J and Thompson S M 2021 *Thermal Monitoring and Modeling of Ti–6Al–4V Thin Wall Temperature Distribution during Blown Powder Laser Directed Energy Deposition (volume 1: Additive Manufacturing; Advanced Materials Manufacturing; Biomanufacturing; Life Cycle Engineering; Manufacturing Equipment and Automation)* (Virtual, Online: American Society of Mechanical Engineers (ASME)) p V001T01A008) (accessed 29 September 2021)
[43] Lim A, Castagne S and Cher Wong C 2016 Effect of deep cold rolling on residual stress distributions between the treated and untreated regions on Ti–6Al–4V alloy *J. Manuf. Sci. Eng.* **138** 111005
[44] Hibbitt D. and Sorrensen P. 2014 *Abaqus Analysis User's Manual 6.14. Dassault Systemes Simulia Corp., Providence, RI*
[45] Goldak J, Chakravarti A and Bibby M 1984 A new finite element model for welding heat sources *Metall. Trans.* B **15** 299–305
[46] Deng D 2009 FEM prediction of welding residual stress and distortion in carbon steel considering phase transformation effects *Mater. Des.* **30** 359–66
[47] Ni J, Wang X, Gong J and Abdel Wahab M 2018 Thermal, metallurgical and mechanical analysis of circumferentially multi-pass welded P92 steel pipes *Int. J. Press. Vessels Pip.* **165** 164–75



https://dspace.org/

Efficient determination and evaluation of steady-state thermal-mechanical variables generated by wire arc additive manufacturing and high pressure rolling

Gornyakov, Valeriy; Sun, Yongle; Ding, Jialuo; Williams, Stewart W.

2021-11-02
IOP Publishing
https://doi.org/10.1088/1361-651X/ac35b8
Gornyakov V, Sun Y, Ding J, Williams S. (2022) Efficient determination and evaluation of steady-state thermal-mechanical variables generated by wire arc additive manufacturing and high pressure rolling, Modelling and Simulation in Materials Science and Engineering, Volume 30, Issue 1, January 2022, Article number 014001

Downloaded from a DSpace repository. https://dspace.org/